Inorg. Chem. **2008**, *47*, 2552−2561

Spin-Crossover Behavior in Cyanide-bridged Iron(II)−Gold(I) Bimetallic 2D Hofmann-like Metal−Organic Frameworks§

Gloria Agustí,[†] M. Carmen Muñoz,[‡] Ana B. Gaspar,[†] and José A. Real*[,†]

Institut de Ciència Molecular/Departament de Química Inorgànica, Universitat de València, Edificios de Institutos de Paterna, P.O. Box 22085, 46071, València, Spain, and Departament de Física Aplicada, Universitat Politècnica de València, Camino de Vera s/n, 46022, València, Spain

Received September 20, 2007

The synthesis and characterization of new two-dimensional (2D) cyanide-bridged iron(II)−gold(I) bimetallic coordination polymers formulated, $\{Fe(3\text{-}Xpy)_2[Au(CN)_2]_2\}$ (py = pyridine; X = F (**1**), Cl (**2**), Br (**3**), and I (**4**)) and the clathrate derivative $\{Fe(3\text{-}Ipy)_2[Au(CN)_2]_2\}\cdot 1/2(3\text{-}Ipy)$ (**5**), are reported. The iron(II) ion lies in pseudooctahedral $[FeN_6]$ sites defined by four $[Au(CN)_2]^-$ bridging ligands and two 3-Xpy ligands occupying the equatorial and axial positions, respectively. Although only compounds **2** and **4** can be considered strictly isostructurals, all of the components of this family are made up of parallel stacks of corrugated $\{Fe[Au(CN)_2]_2\}_n$ grids. The grids are formed by edge sharing of $\{Fe_4[Au(CN)_2]_4\}$ pseudosquare moieties. The stacks are constituted of double layers sustained by short aurophilic contacts ranging from 3.016(2) to 3.1580(8) Å. The Au···Au distances between consecutive double layers are in the range of 5.9562(9)−8.790(2) Å. Compound **5**, considered a clathrate derivative of **4**, includes one-half of a 3-Ipy molecule per iron(II) atom between the double layers. Compound **1** undergoes a half-spin transition with critical temperatures $T_c\downarrow = 140$ K and $T_c\uparrow = 145$ K. The corresponding thermodynamic parameters derived from differential scanning calorimetry (DSC) are $\Delta H = 9.8 \pm 0.4$ kJ mol^{-1} and $\Delta S = 68.2 \pm 3$ J K mol^{-1}. This spin transition is accompanied by a crystallographic phase transition from the monoclinic $P2_1/c$ space group to the triclinic $P\bar{1}$ space group. At high temperatures, where **1** is 100% high-spin, there is only one crystallographically independent iron(II) site. In contrast, the low temperature structural analysis shows the occurrence of two crystallographically independent iron(II) sites with equal population, one high-spin and the other low-spin. Furthermore, **1** undergoes a complete two-step spin transition at pressures as high as 0.26 GPa. Compounds **2**−**4** are high-spin iron(II) complexes according to their magnetic and $[FeN_6]$ structural characteristics. Compound **5**, characterized for having two different iron(II) sites, displays a two-step spin transition with critical temperatures of $T_c^1 = 155$ K, $T_c^2\downarrow = 97$ K, and $T_c^2\uparrow = 110$ K. This change of spin state takes place in both sites simultaneously. All of these results are compared and discussed in the context of other $\{Fe(L)_x[M^I(CN)_2]\}$ coordination polymers, particularly those belonging to the homologous compounds $\{Fe(3\text{-}Xpy)_2[Ag(CN)_2]_2\}$ and their corresponding clathrate derivatives.

Introduction

The search for new molecular materials able to manifest a bistable behavior is an issue of permanent interest in the chemistry and physics of materials because they can be envisaged as basic components of new memory and sensory devices.[1] It is well-known that one of the most spectacular examples of bistability in molecular science stems from iron(II) spin crossover (SCO) complexes.[2] They reversibly change between two electronic states, low-spin (LS) and high-spin (HS), induced by an external action such as temperature, pressure,[3] light irradiation,[4] pulsed magnetic fields,[5] and even an analyte[6] (typically solvent molecules).

Since some years after the discovery of the first Hofmann-like iron(II) SCO coordination polymer, $\{Fe(pyridine)_2[Ni(CN)_4]\}$,[7] we have been systematically investigating the

§ Dedicated to the memory of Professor Xavier Solans Huguet.

* To whom correspondence should be addressed. E-mail: jose.a.real@uv.es.

† Universitat de València.

‡ Universitat Politècnica de València.

(1) Lehn, J. M. *Science* **2002**, *295*, 2400.

10.1021/ic701865k CCC: $40.75
Published on Web 02/23/2008

synthesis, characterization, and SCO properties of new polymeric Hofmann-like compounds. In general, combination of an Fe(II) ion with a monodentate or bis-monodentate pyridine-like ligand and $[M^{II}(CN)_4]^{2-}$ (M^{II} = Ni, Pd, and Pt) anions affords highly insoluble two- (2D) or three-dimensional (3D) SCO coordination polymers, which usually display cooperative spin transitions with hysteresis (bistability) and are accompanied by drastic color changes.[8] It is worth mentioning that the 3D polymers {Fe(pyrazine)$[M^{II}(CN)_4]$} (M^{II} = Ni, Pd, and Pt) display stable discontinuous spin transitions with hysteresis ca. 25–30 K wide around room temperature, after annealing the samples at ca. 423 K.[6c,d,9] These compounds gather some additional properties that make them very singular materials. For instance, they are nanoporous frameworks, and consequently, their SCO properties depend dramatically on the number of guest solvent molecules allocated in the pores.[6c] It has also been proven on the Pt derivative that the spin transition can be switched, within the hysteresis loop, by irradiating the sample with a pulse of light at room temperature.[9] This is a desirable but uncommon property in SCO materials as, in general, the photoinduced metastable HS state decays very fast at temperatures higher than at 60 K.[4] It has also been demonstrated that their SCO properties remain when these polymers are grown as thin layers of nanometric thickness,[10] and more recently, it has been proven that these thin layers are processable via nanoscale size patterning of small {Fe(pyrazine)$[Pt(CN)_4]$} dots.[11]

The use of simpler anionic metal-complexes, $[M^{I}(CN)_2]^-$ (M^{I} = Cu, Ag, and Au) as bridging ligands enabled us to do the synthesis of an important number of 1–3D frameworks with a rich variety of topologies and SCO behaviors.[6b,12] In this respect, only two polymers of distinct dimensionality made up of Fe(II), $[Cu(CN)_2]^-$ and 3-CNpyridine (1D)[12h] or pyrimidine (2D)[12b] have been reported. However, a great variety of compounds constituted of 2D or single, double or triple-interpenetrated 3D networks have been obtained using $[Ag(CN)_2]^-$ or $[Au(CN)_2]^-$ as bridging anions together with Fe(II) and ligands like pyrazine,[12a] 4,4′-bipy,[12a] bispyridylethylene,[12a] pyrimidine,[6b,12e–g] or 3-CNpyridine.[12c,d,i]

In the search for new SCO polymers with interesting properties, we have undertaken, more recently, the synthesis and characterization of new iron(II) based Hofmann-like coordination polymers using the organic ligand 3-Xpyridine (X = F, Cl, Br, and I) and the bridging metallo-anionic ligand $[M^{I}(CN)_2]^-$ (M^{I} = Cu, Ag, and Au) as counterions. The $[Ag(CN)_2]^-$ derivatives have been reported recently,[13] and as a second part of this study, we report here the synthesis, crystal structures, and magnetic and calorimetric characterization of {Fe(3-Xpy)$_2$[Au(CN)$_2$]$_2$} (py = pyridine; X = F, Cl, Br, and I) 2D coordination polymers and the clathrate derivative {Fe(3-Ipy)$_2$[Au(CN)$_2$]$_2$}·1/2(3-Ipy).

Experimental Section

Materials. $FeCl_2 \cdot 4H_2O$, 3-Xpy (X = F, Cl, Br, and I) and $K[Au(CN)_2]$ were purchased from commercial sources and were used as received.

Preparation of 1–5. These compounds were synthesized by slow diffusion of two methanol–water (1:1) solutions, one containing a mixture (2 mL) of $FeCl_2 \cdot 4H_2O$ (0.25 mmol, 49.7 mg) and 3-Xpy (1 mmol, 97.09 mg (X = F), 113.54 mg (X = Cl), 158 mg (X = Br), and 205 mg (X = I)) in one side of the H-shaped vessel. The other side contained 2 mL of a solution of $K[Au(CN)_2]$ (0.5 mmol, 144.05 mg). Then, the H-shaped vessel was filled with a methanol–water solution (1:1). Pale-yellow single crystals of **1–5** were formed over a period of two weeks. All manipulations were performed under an argon atmosphere. Given that **4** and **5** usually grow simultaneously in the same reaction vessel and have the same color, it is rather common to get samples containing mixtures of crystals of both compounds. This is clearly evidenced from the magnetic properties of the pure compounds as **4** is purely HS and **5** undergoes a characteristic two-step spin transition at well-defined critical temperatures. Separation of pure, single crystals of each compound has been possible using a binocular lens because they differ in shape; namely, crystals of **4** are long rectangular needles, and crystals of **5** have a cubic shape. Anal. Calcd for $C_{14}H_8N_6F_2Au_2Fe$ (**1**): C, 22.48; H, 1.08; N, 11.23. Found: C, 22.17; H, 1.04; N, 11.29 (yield ca. 65%). Anal. Calcd for $C_{14}H_8N_6Cl_2Au_2Fe$ (**2**): C, 21.53; H, 1.03; N, 10.76. Found: C, 21.41; H, 1.05; N, 10.89 (yield ca. 70%). Anal. Calcd for $C_{14}H_8N_6Br_2Au_2Fe$ (**3**): C, 19.33; H, 0.93; N, 9.66. Found: C, 19.41; H, 0.98; N, 9.71 (yield ca. 70%). Anal. Calcd for $C_{14}H_8N_6I_2Au_2Fe$ (**4**): C, 17.45; H, 0.84; N, 8.72. Found: C, 17.53; H, 0.83; N, 8.63 (yield ca. 50%). Anal.

(2) (a) Spin Crossover in Transition Metal Compounds. *Top. Curr. Chem.*; Gütlich, P.; Goodwin, H. A., Eds.; Springer: New York, 2004; Vols. *233, 234, 235*. (b) Gütlich, P.; Hauser, A.; Spiering, H. *Angew. Chem., Int. Ed. Engl.* **1994**, *33*, 2024. (c) Real, J. A.; Gaspar, A. B.; Muñoz, M. C. *Dalton Trans.* **2005**, 2062. (d) Gaspar, A. B.; Ksenofontov, V.; Seredyuk, M.; Gütlich, P. *Coord. Chem. Rev.* **2005**, *249*, 2661. (e) Real, J. A.; Gaspar, A. B.; Niel, V.; Muñoz, M. C. *Coord. Chem. Rev.* **2003**, *236*, 121.

(3) Ksenofontov, V.; Gaspar, A. B.; Gütlich, P. *Top. Curr. Chem.* **2004**, *235*, 23.

(4) Hauser, A. *Top. Curr. Chem.* **2004**, *234*, 155.

(5) Bousseksou, A.; Varret, F.; Goiran, M.; Boukheddaden, K.; Tuchagues, J. P. *Top. Curr. Chem.* **2004**, *235*, 65.

(6) (a) Halder, G. J.; Kepert, C. J.; Moubaraki, B.; Murray, K. S.; Cashion, J. D *Science* **2002**, *298*, 1762. (b) Niel, V.; Thompson, A. L.; Galet, A.; Muñoz, M. C.; Goeta, A. E.; Real, J. A. *Angew. Chem., Int. Ed* **2003**, *42*, 3760. (c) Galet A. PhD. Thesis; Universitat de València, València, Spain, 2007. (d) Tayagaki, T.; Galet, A; Molnár, G.; Muñoz, M. C.; Zwick, A.; Tanaka, K.; Real, J. A.; Bousseksou, A. *J. Phys. Chem. B* **2005**, *109*, 14859.

(7) Kitazawa, T.; Gomi, Y.; Takahashi, M.; Takeda, M.; Enemoto, A.; Miyazaki, T.; Enoki, T. *J. Mater. Chem.* **1996**, *6*, 119.

(8) Niel, V.; Martinez-Agudo, J. M.; Muñoz, M. C.; Gaspar, A. B.; Real, J. A. *Inorg. Chem.* **2001**, *40*, 3838.

(9) Bonhommeau, S.; Molnár, G.; Galet, A.; Zwick, A.; Real, J. A.; McGarvey, J. J.; Bousseksou, A. *Angew. Chem., Int. Ed.* **2005**, *44*, 4069.

(10) Cobo, S.; Molnár, G.; Real, J. A.; Bousseksou, A. *Angew. Chem., Int. Ed.* **2006**, *45*, 5786.

(11) Molnár, G.; Cobo, S.; Real, J. A.; Carcenac, F.; Daran, E.; Vieu, C.; Bousseksou, A. *Adv. Mater.* **2007**, *19*, 2163.

(12) (a) Niel, V.; Muñoz, M. C.; Gaspar, A. B.; Galet, A.; Levchenko, G.; Real, J. A. *Chem.−Eur. J.* **2002**, *8*, 2446. (b) Niel, V.; Galet, A.; Gaspar, A. B.; Muñoz, M. C.; Real, J. A. *Chem. Commun.* **2003**, 1248. (c) Galet, A.; Niel, V.; Muñoz, M. C.; Real, J. A *J. Am. Chem. Soc.* **2003**, *125*, 14224. (d) Galet, A.; Muñoz, M. C.; Martínez, V.; Real, J. A. *Chem. Commun.* **2004**, 2268. (e) Niel, V.; Thompson, A. L.; Goeta, A. E.; Enachescu, C.; Hauser, A.; Galet, A.; Muñoz, M. C.; Real, J. A. *Chem.−Eur. J.* **2005**, *11*, 2047. (f) Galet, A.; Gaspar, A. B.; Muñoz, M. C.; Bukin, G. V.; Levchenko, G.; Real, J. A. *Adv. Mater.* **2005**, *17*, 2949. (g) Galet, A.; Muñoz, M. C.; Gaspar, A. B.; Real, J. A *Inorg. Chem.* **2005**, *44*, 8749. (h) Galet, A.; Muñoz, M. C.; Real, J. A *Inorg. Chem.* **2006**, *45*, 4583. (i) Galet, A.; Muñoz, M. C.; Real, J. A. *Chem. Commun.* **2006**, 4321.

(13) Muñoz, M. C.; Gaspar, A. B.; Galet, A.; Real, J. A. *Inorg. Chem.* **2007**, *46*, 8182.

Table 1. Crystal Data for **1**, **3**, and **4**

	1 (293 K)	**1** (120 K)	**3**	**4**
empirical formula	$C_{14}H_8N_6F_2Au_2Fe$	$C_{28}H_{16}N_{12}F_4Au_4Fe_2$	$C_{14}H_8N_6Br_2Au_2Fe$	$C_{28}H_{16}N_{12}I_4Au_4Fe_2$
mol wt	748.05	1496.10	869.87	1927.70
crystal system	monoclinic	triclinic	monoclinic	triclinic
space group	$P2_1/c$	$P\bar{1}$	$P2_1/c$	$P\bar{1}$
a (Å)	9.0300(4)	8.9010(4)	9.3950(5)	10.5380(2)
b (Å)	13.8630(5)	13.5400(6)	15.5720(9)	12.9200(3)
c (Å)	15.4510(7)	15.2400(8)	14.1100(9)	15.7420(4)
α (deg)		89.787(2)		87.8420(10)
β (deg)	96.255(2)	96.469(2)	105.323(3)	87.5680(10)
γ (deg)		91.835(2)		84.6320(10)
V (Å^3)	1922.69(14)	1824.09(15)	1990.9(2)	2130.74(8)
Z	4	2	4	2
D_c (mg cm^{-3})	2.584	2.724	2.902	3.005
F(000)	1344		1552	1696
μ(Mo Kα) (mm^{-1})	15.994	16.858	19.443	17.315
crystal size (mm)	0.04 × 0.06 × 0.06		0.04 × 0.04 × 0.09	0.04 × 0.08 × 0.08
No. of total reflections	4242	7870	4522	9561
No. of reflections [$I > 2\sigma(I)$]	2411	4897	2398	6561
R_1 [$I > 2\sigma(I)$][a]	0.0553	0.1649	0.0772	0.0526
wR [$I > 2\sigma(I)$][a]	0.1268	0.3673	0.1962	0.1196
S	0.960	0.978	1.069	0.887

[a] $R_1 = \Sigma||Fo| - |F||/\Sigma|F_o|$; $wR = [\Sigma[w(F_o^2 - F_c^2)^2]/\Sigma[w(F_o^2)^2]]^{1/2}$; $w = 1/[\sigma^2(F_o^2) + (mP)^2 + nP]$ where $P = (F_o^2 + 2F_c^2)/3$; m = 0.0778 (**1**), 0.0766 (**1** (120 K)), 0.1300 (**3**), and 0.0896 (**4**); n = 0.0000 (**1**), 1723.5553 (**1** (120 K)), 0.0000 (**3**), and 0.0000 (**4**)

Calcd for $C_{16.5}H_{10}N_{6.5}I_{2.5}Au_2Fe$ (**5**): C, 18.58; H, 0.95; N, 8.54. Found: C, 18.12; H, 1.01; N, 8.71 (yield ca. 15%).

Magnetic Measurements. The variable temperature magnetic susceptibility measurements were carried out on samples constituted by small crystals (20–30 mg) using a Quantum Design MPMS2 SQUID susceptometer equipped with a 5.5 T magnet and operating at 1 T and 1.8–400 K. Magnetic measurements under hydrostatic pressure were performed using a cell made of hardened beryllium bronze with silicon oil as the pressure transmitting medium operates in the pressures range 10^5 Pa < P < 0.14 GPa (accuracy ≈ ±0.025 GPa). Cylindrically shaped powder sample holders with dimensions of 1 mm in diameter and 5–7 mm in length were used. The pressure was measured using the pressure dependence of the superconducting transition temperature of a built-in pressure sensor made of high purity tin.[14] The susceptometer was calibrated with $(NH_4)_2Mn(SO_4)_2 \cdot 12H_2O$. Experimental susceptibilities were corrected for diamagnetism of the constituent atoms by the use of Pascal's constants.

Differential Scanning Calorimetry (DSC). Calorimetric measurements have been performed on **1** using a differential scanning calorimeter (Mettler Toledo DSC 821^e). Low temperatures were obtained with an aluminum block attached to the sample holder, refrigerated with a flow of liquid nitrogen and stabilized at a temperature of 110 K. The sample holder was kept in a dry box under a flow of dry nitrogen gas to avoid water condensation. The measurements were carried out using about 15 mg of powdered sample sealed in aluminum pans with a mechanical crimp. Temperature and heat flow calibrations were made with standard samples of indium by using its melting (429.6 K, 28.45 J g^{-1}) transition. An overall accuracy of ± 0.2 K in temperature and ± 2% in the heat capacity is estimated. The uncertainty increases for the determination of the anomalous enthalpy and entropy because of the subtraction of an unknown baseline.

X-ray Crystallography. Single crystal X-ray diffraction data were collected at 293 and 120 K for **1**, at 293 K for **2**−**4**, and at 293, 130, and 80 K for **5** using a Nonius Kappa-CCD single crystal diffractometer using Mo Kα (λ = 0.71073 Å). A multiscan absorption correction was performed but not applied. The absorption correction was found to have no significant effect on the refinement results. The structures were solved by direct methods using SHELXS-97 and were refined by full-matrix least-squares on F^2 using SHELXL-97.[15] All nonhydrogen atoms were refined anisotropically, except for compound **1** at 120 K and **5** at 130 K, in which only Fe and Au atoms were refined anisotropically. The low quality of crystal data of **1** at 120 K is due to the occurrence of a sharp phase transition that provokes a notable increase of the mosaicity of the crystals in the low temperature phase. Although the high-temperature spin transition is not so discontinuous for **5**, the mosaicity also increases significantly just in the middle of the plateau (130 K) between the two spin-change steps, making these data of less quality than that at 293 and 80 K. Relevant crystallographic data and selected bond lengths for **1** and **3**−**5** are displayed in Tables 1−4.

Crystal Structure of 1 and 3 (T = 293 K). Compounds **1** and **3** display the monoclinic $P2_1/c$ space group at 293 K. Their crystal structures are tightly related but are not identical. Despite this, we have considered the same atom numbering for both compounds (see Figure 1). They are made up of a stack of infinite grids formed by the assembly of $[Au(CN)_2]^-$ bridging ligands and Fe(II) centers. Each Fe(II) center defines a distorted elongated octahedron with four equatorial positions occupied by the nitrogen atoms of two crystallographically independent $[Au(CN)_2]^-$ ligands, the bond distances are Fe−N(3) = 2.148(11) [2.12(2)] Å, Fe−N(4) = 2.167(9) [2.16(2)] Å, Fe−N(5) = 2.152(10) [2.15(2)] Å, Fe−N(6) = 2.139(10) [2.16(2)] Å for **1** and [**3**], respectively. The axial positions are occupied by two 3-Xpy ligands (X = F and Br), the corresponding Fe−N bond distances are Fe−N(1) = 2.263(12) [2.24(2)] Å and Fe−N(2) = 2.229(12) [2.29(2)] Å for **1** and [**3**], respectively. These Fe−N bond lengths are consistent with the expected values for an iron(II) ion in the high spin (HS) state (see Table 3).

The 3-Xpy groups are in a trans orientation with respect to the N(1)−Fe−N(2) axis. A projection of them on the equatorial plane bisects the FeN(5)N(6) and FeN(3)N(4) quadrants defining two different angles (ca. 26.5 and 62.8°) in **1**. Furthermore, the F(2) atom is disordered, showing 50% occupancy between the C(9) and

(14) Baran, M.; Dyakonov, V. P.; Gladczuk, L.; Levchenko, G. G.; Piechota, S.; Szymczak, G. *Physica C* **1995**, *241*, 383.

(15) Sheldrick, G. M. *SHELX97: Program for Crystal Structure Determination.* University of Gottingen, Germany, 1997.

Table 2. Crystal Data for **5**

	293 K	130 K	80 K
empirical formula	$C_{33}H_{20}N_{13}I_5Au_4Fe_2$		
mol wt	2132.69		
crystal system	monoclinic		
space group	$P2_1/c$		
a (Å)	23.5190(5)	23.1960(4)	22.9800(3)
b (Å)	14.3220(3)	14.1440(4)	13.9160(3)
c (Å)	15.3060(3)	15.0240(6)	14.7240(5)
α (deg)			
β (deg)	106.8220(10)	107.1820(10)	106.6790(10)
γ (deg)			
V (Å^3)	4935.0(2)	4709.2(2)	4510.5(2)
Z	4		
D_c (mg cm^{-3})	2.870	3.008	3.141
F(000)	3768		
μ(Mo Kα) (mm^{-1})	15.585	16.332	17.052
crystal size (mm)	0.05 × 0.05 × 0.05		
No. of total reflections	11237	10417	10304
No. of reflections [$I > 2\sigma(I)$]	6612	7428	7049
R_1 [$I > 2\sigma(I)$][a]	0.0527	0.1182	0.0435
wR [$I > 2\sigma(I)$][a]	0.1065	0.2401	0.0926
S	1.000	1.190	1.005

[a] $R_1 = \Sigma||Fo| - |F||/\Sigma|F_o|$; $wR = [\Sigma[w(F_o^2 - F_c^2)^2]/\Sigma[w(F_o^2)^2]]^{1/2}$; $w = 1/[\sigma^2(F_o^2) + (mP)^2 + nP]$ where $P = (F_o^2 + 2F_c^2)/3$; $m = 0.0404$ (**5**), 0.0000 (**5** (130 K)), and 0.0400 (**5** (80 K)); $n = 32.7577$ (**5**), 1080.6865 (**5** (130 K)) and 39.8124 (**5** (80 K)).

Table 3. Selected Bond Lengths (Å) for **1**, **3**, and **4**

	1 (293 K)	**1** (120 K)	**3**	**4**
Fe−N(1)	2.263(12)		2.24(2)	
Fe−N(2)	2.229(12)		2.29(2)	
Fe−N(3)	2.148(11)		2.12(2)	
Fe−N(4)	2.167(9)		2.16(2)	
Fe−N(5)	2.152(10)		2.15(2)	
Fe−N(6)	2.139(10)		2.16(2)	
Fe(1)−N(1)		2.25(5)		2.268(11)
Fe(1)−N(2)		2.19(4)		2.220(11)
Fe(1)−N(3)		2.17(4)		2.113(11)
Fe(1)−N(4)		2.12(5)		2.134(10)
Fe(1)−N(5)		2.15(4)		2.139(10)
Fe(1)−N(6)		2.13(5)		2.124(10)
Fe(2)−N(7)		2.02(4)		2.235(12)
Fe(2)−N(8)		2.03(4)		2.236(12)
Fe(2)−N(9)		1.96(5)		2.116(10)
Fe(2)−N(10)		1.98(4)		2.171(10)
Fe(2)−N(11)		1.90(5)		2.174(9)
Fe(2)−N(12)		1.97(5)		2.161(10)
Au(1)−C(11)	2.011(13)		2.02(2)	
Au(1)−C(14)	1.972(12)		1.98(2)	
Au(2)−C(12)	1.962(12)		1.96(2)	
Au(2)−C(13)	1.989(12)		1.99(2)	
Au(1)−C(11)		1.99(5)		
Au(1)−C(25)		1.96(5)		
Au(2)−C(12)		2.00(5)		
Au(2)−C(26)		1.97(5)		
Au(3)−C(13)		2.01(5)		
Au(3)−C(27)		2.00(5)		
Au(4)−C(14)		1.98(5)		
Au(4)−C(28)		2.00(6)		
Au(1)−C(11)				1.983(12)
Au(1)−C(25)				2.000(11)
Au(2)−C(26)				2.007(14)
Au(2)−C(28)				1.987(13)
Au(3)−C(13)				1.988(12)
Au(3)−C(27)				1.985(14)
Au(4)−C(12)				1.981(12)
Au(4)−C(14)				1.983(12)

C(7) atoms; only one of the two positions is shown in Figure 1. At variance with **1**, the axial N(1)−Fe−N(2) axis significantly differs from linearity, with an angle of 171.4(6)° (this angle is 178.9(3)° for **1**), and the two 3-Brpy ligands project almost perfectly on the N(3)−Fe−N(5) equatorial bonds in **3**.

Table 4. Selected Bond Lengths [Å] and Angles [°] for **5**

	293 K	**130 K**	**80 K**
Fe(1A)−N(1)	2.230(10)	2.12(3)	2.023(8)
Fe(1A)−N(2)	2.241(10)	2.12(3)	2.026(9)
Fe(1A)−N(3)	2.144(9)	2.02(3)	1.942(9)
Fe(1A)−N(4)	2.151(9)	2.05(3)	1.961(8)
Fe(1A)−N(5)	2.143(9)	2.06(3)	1.929(8)
Fe(1A)−N(6)	2.148(9)	2.04(3)	1.930(8)
Fe(1B)−N(1)	2.244(9)	2.16(2)	2.020(8)
Fe(1B)−N(2)	2.228(9)	2.16(3)	2.020(8)
Fe(1B)−N(3)	2.179(9)	2.02(3)	1.958(9)
Fe(1B)−N(4)	2.144(10)	2.07(3)	1.958(9)
Fe(1B)−N(5)	2.134(9)	2.04(3)	1.946(8)
Fe(1B)−N(6)	2.152(9)	2.05(3)	1.951(9)
Au(1A)−C(11A)	1.985(11)	1.93(3)	2.006(10)
Au(1A)−C(14A)	1.986(11)	1.99(3)	2.012(11)
Au(2A)−C(12A)	1.962(12)	2.05(3)	1.991(10)
Au(2A)−C(13A)	1.989(11)	1.98(4)	2.015(10)
Au(1B)−C(11B)	1.990(12)	2.05(3)	1.995(10)
Au(1B)−C(14B)	1.967(12)	1.93(3)	1.992(10)
Au(2B)−C(12B)	1.963(11)	1.92(3)	1.985(10)
Au(2B)−C(13B)	2.012(12)	2.02(4)	1.992(11)

The two $[Au(CN)_2]^-$ are almost linear, the angles defined by C(14)−Au(1)−C(11) and C(13)-Au(2)−C(12) are, respectively, 177.6(6) [175.6(8)]° and 178.0(6) [176.7(9)]° for **1** and [**3**]. However, the Fe−N(3)−C(11), Fe−N(4)−C(12), Fe−N(5)−C(13), and Fe−N(6)−C(14) angles are more bent in **1** [169.7(12)°, 167.5(12)°, 171.8(11)° and 167.9(12)°, respectively] than in **3** [173(2)°, 175.8(14)°, 170(2)° and 178.2(15)°, respectively]. This confers a markedly more undulating shape to the $[Fe-NC-Ag-CN-Fe]_\infty$ chains in **1**. Interestingly, adjacent parallel chains display an opposed phase. Furthermore, an almost orthogonal set of parallel $[Fe-NC-Ag-CN-Fe]_\infty$ chains met at the Fe(II) centers defining nearly square-shaped 10.39(2) × 10.37(2) [10.52(3) × 10.49(3)] Å windows in **1** and [**3**], respectively. The resulting corrugated 2D grids stack along the [100] direction. They interact by pairs defining double layers sustained by strong aurophilic interactions: Au(1)···Au(2)^{i} = 3.1580(8) [3.0981(13)] Å ($i = -x$, ½ + y, ½ − z) for **1** and [**3**], respectively (Figure 2a). The Au(1)···Au(2)^{ii} distance between two adjacent noninteracting layers is 5.9562(9) [6.300(2)] Å (ii = 1 − x, −½ + y, ½ − z) for **1** and [**3**], respectively (Figure 2b). The space between them is filled with the 3-Xpy rings. The 3-Fpy groups of layers **A** and **C** interact via

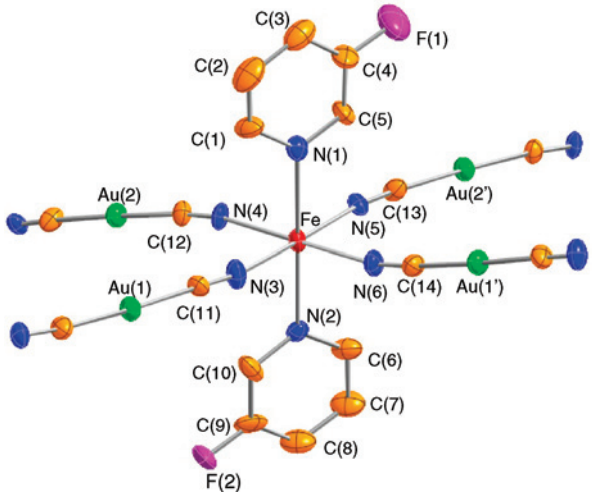

Figure 1. ORTEP representation of a fragment of **1** containing its asymmetric unit and atom numbering at 293 K. The structure of **3** is tightly related to that of **1** (see text). Consequently, we have used the same ORTEP representation for both compounds. Thermal ellipsoids are presented at 30% of probability.

π-stacking (Figure 2b). The corresponding significant distances smaller than the sum of the van der Waals radius (ca. 3.70 Å) are gathered in Table 5. There are no significant F···F contacts.

In **3**, the number of intermolecular C···C contacts is significantly smaller as compared to **1** (C(3)···C(10)^{i} = 3.47(4) Å, C(2)···C(12)^{i} = 3.62(4) Å (i = 1 + x, y, z)). In contrast, **3** displays short Br(1)···Br(2)^{ii} contacts, 3.777(6) Å (ii = 1 − x, ½ + y, $^5/_2$ − z), which are smaller than the double of the van der Waals radius (ca. 3.90 Å).

Crystal Structure of 1 (T = 120 K). Compound **1**undergoes a spin transition at around 140 K; consequently, we have studied its structure at 120 K. At this temperature the crystal displays the triclinic $P\bar{1}$ space group. As a consequence of the sharp phase transition, the mosaicity of the crystal increased significantly in the low temperature phase. This fact prevents us from obtaining a typical accuracy level for the structural data. Despite this problem, the data clearly indicates that, in contrast to the high temperature structure, there are two crystallographically distinct Fe(II) atoms: (i) the Fe(1) site defines an axially elongated octahedron similar to that described at 293 K [Fe(1)−N(1) = 2.25(5) Å, Fe(1)−N(2) = 2.19(4) Å, Fe(1)−N(3) = 2.17(4) Å, Fe(1)−N(4) = 2.12(5) Å, Fe(1)−N(5) = 2.15(4) Å, and Fe(1)−N(6) = 2.13(5) Å]; and (ii) the Fe(2) site defines a rather regular octahedron with significantly shorter metal-to-ligand bond distances [Fe(2)−N(7) = 2.02(4) Å, Fe(2)−N(8) = 2.03(4) Å, Fe(2)−N(9) = 1.96(5) Å, Fe(2)−N(10) = 1.98(4) Å, Fe(2)−N(11) = 1.90(5) Å and Fe(2)−N(12) = 1.97(5) Å]. These Fe−N bond lengths correspond quite well to those expected for an Fe(II) ion in the HS and LS spin state for Fe(1) and Fe(2), respectively (Figure 3). The variation of the average [FeN_6] distances with respect to the 293 K structure is ca. 0.02 Å for Fe(1) and ca. 0.21 Å for Fe(2). The former variation is insignificant, whereas the latter corresponds to the variation expected for a HS-to-LS spin state change. These results also agree well with the magnetic properties observed for this compound (vide infra).

There are four crystallographically distinct $[Au(CN)_2]^-$ groups, which generate two slightly different intermetallic interactions in the double layers: Au(1)···Au(4) = 3.082(3) Å and Au(2)···Au(3) = 3.124(3) Å. The HS-to-LS state change observed in the Fe(2) site also significantly modifies the Fe−NC−Au−CN−Fe distances (average 10.19(2) Å) but not the angles of the $\{Fe[Au(CN)_2]_4$

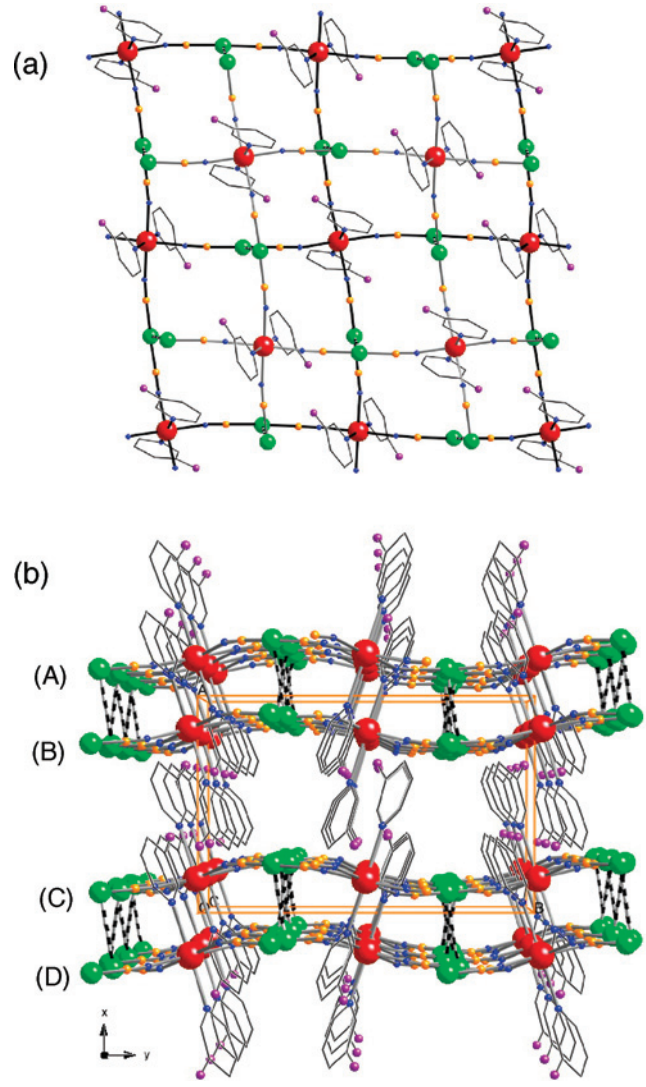

Figure 2. (a) View of the relative disposition of two grids of **1** (**3**) emphasizing the aurophilic interactions (dotted bars). (b) Stacking of four consecutive layers of **1** (**3**) along [100] direction.

windows. It is worthwhile to mention that Fe(1) and Fe(2) sites alternate along the near orthogonal sets of parallel [Fe−NC−Au−CN−Fe]$_\infty$ chains mentioned above; hence, each HS or LS site is surrounded by four sites exhibiting the opposite spin state.

Table 5. Selected Intermolecular Contacts [Å] for **1**, **3** and **4**

	1 (293 K)	**1** (120 K)	**3**	**4**
C(3)···C(6)^{i}	3.46(3)	3.44(9)		
C(4)···C(6)^{i}	3.66(3)	3.63(9)		
C(4)···C(7)^{i}	3.54(3)	3.59(9)		
C(2)···C(9)^{i}	3.67(3)	3.46(9)		
C(1)···C(8)^{i}	3.56(3)	3.34(8)		
C(1)···C(9)^{i}	3.74(3)	3.62(8)		
C(5)···C(7)^{i}	3.73(3)	3.60(8)		
C(2)···C(12)^{i}			3.62(4)	
C(3)···C(10)^{i}			3.47(4)	
C(3)···C(12)^{i}			3.56(3)	
C(2)···C(22)^{ii}				3.44(2)
C(3)···C(22)^{ii}				3.50(2)
C(3)···C(23)^{ii}				3.51(2)
Br(1)···Br(2)^{iii}			3.777(6)	
I(2)···I(4)^{iv}				4.072(2)
I(3)···I(4)^{v}				4.047(2)

^{i} = 1 + x, y, z; ^{ii} = x, y − 1, z; ^{iii} = 1 − x, ½ + y, $^5/_2$ − z; ^{iv} = 2 − x, 2 − y, −z; ^{v} = 1 − x, 2 − y, 1 − z.

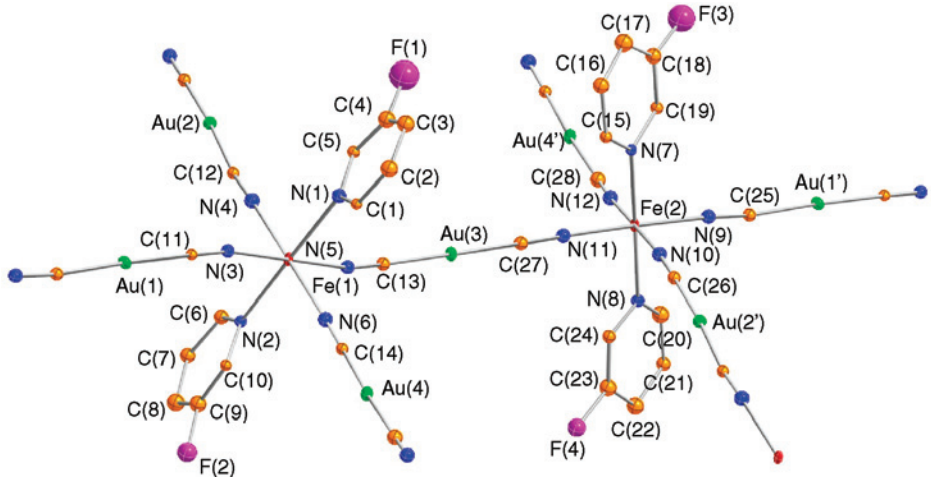

Figure 3. ORTEP representation of a fragment of **1** containing its asymmetric unit and atom numbering at 120 K. Thermal ellipsoids are presented at 30% of probability.

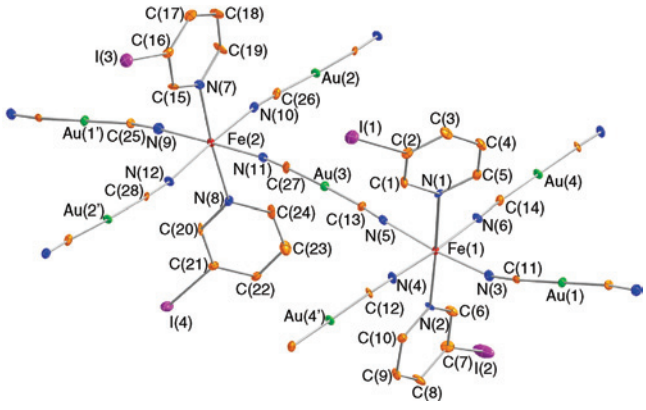

Figure 4. ORTEP representation of a fragment of **2** and **4** containing its asymmetric unit and atom numbering. Thermal ellipsoids are presented at 30% of probability.

At 120 K the C···C distances become shorter, indicating an increase of intensity of the π-stacking interactions (Table 5). However, there are no significant F···F contacts.

Crystal Structure of Compounds 2 and 4. Compounds **2** and **4** are isostructural and crystallize in the triclinic $P\bar{1}$ space group. The crystal structure of **2** was solved, but the crystals obtained from different batches were not good enough to get *R*-values smaller than 17% (see Supporting Information). Consequently, here we only will describe in detail the structure of **4**. The crystal structure of both compounds is similar to that described for **1** at 120 K; however, they are fully HS in the whole range of temperature. There are two crystallographically different Fe(II) atoms defining distorted octahedrons (Figure 4) (see Table 3). The axial Fe−3-Xpy bond lengths are longer [Fe(1)−N(1) = 2.268(11) Å, Fe(1)−N(2) = 2.220(11) Å, and Fe(2)−N(7) = 2.235(12) Å, Fe(2)−N(8) = 2.236(12) Å] than the equatorial Fe−NCAu bond lengths [Fe(1)−N(3) = 2.113(11) Å, Fe(1)−N(4) = 2.134(10) Å, Fe(1)−N(5) = 2.139(10) Å, Fe(1)−N(6) = 2.124(10) Å, and Fe(2)−N(9) = 2.116(10) Å, Fe(2)−N(10) = 2.171(10) Å, Fe(2)−N(11) = 2.174(9) Å, Fe(2)−N(12) = 2.161(10) Å]. There are also four crystallographically distinct $[Au(CN)_2]^-$ bridging ligands, which connect the Fe(1) and Fe(2) sites differently, as described for **1** at 120 K. The grid structure can be described as being formed by two near orthogonal sets of parallel $[Fe-NC-Au-CN-Fe]_\infty$ chains. One set is constituted of alternating $[Fe(1)-NC-Au(1)-CN-Fe(1)]_\infty$ and $[Fe(2)-NC-Au(3)-CN-Fe(2)]_\infty$ chains. The other set defines connections between Fe(1) and Fe(2) through $[Au(2)(CN)_2]^-$ and $[Au(4)(CN)_2]^-$, generating a 2D coordination polymer. The crystal packing of **4** (**2**) is also made up of a stacking of double layers. These double layers interact via strong aurophilic interactions [Au(1)···Au(2)^i = 3.0137(8) Å (i = 2 − *x*, 2 − *y*, 1 − *z*) and Au(3)···Au(4)^{ii} = 3.0927(8) Å (ii = 2 − *x*, 1 − *y*, −*z*)]. As in the case of compound **3**, the number of C···C interactions is small as compared with **1** [C(2)···C(22)^i = 3.44(2) Å, C(3)···C(22)^i = 3.50(2) Å, and C(3)···C(23)^i = 3.51(2) Å (i = *x*, *y* − 1, *z*)]. There are also I···I contacts with distances smaller than the double of the van der Waals radius (ca. 4.30 Å): I(2)···I(4)^{ii} = 4.072(2) Å (ii = 2 − *x*, 2 − *y*, −*z*) and I(3)···I(4)^{iii} = 4.047(2) Å (iii = 1 − *x*, 2 − *y*, 1 − *z*).

Crystal Structure of Compound 5. Given that compound **5** undergoes a two-step spin transition (vide infra), its crystal structure has been investigated at three characteristic temperatures: 293, 130 and 80 K. For these temperatures, **5** displays the monoclinic $P2_1/c$ space group. There are two crystallographically distinct Fe(II) atoms, but at difference with structures **1** (low temperature), **2**, and **4**, the two iron sites are not located in alternate positions of each grid but are segregated in different grids. Each double layer contains only one kind of iron site (Fe(A) or Fe(B)), and these double layers alternate in the crystal. Figure 5 displays a representative fragment of the network illustrating the atom numbering around the Fe(A) site. The atom numbering for Fe(B) layers has been kept identical to that of Fe(A) site but with the label B instead of A (see Table 4). Both sites are elongated $[FeN_6]$ octahedrons with two crystallographically distinct 3-Ipy and $[Au(CN)_2]^-$ ligands. The former occupy the axial positions whereas the latter occupy the four equatorial positions. At 293 K, the average Fe−N bond distances are 2.176(10) and 2.180(10) Å for the A and B sites, respectively. These distances are consistent with the observed HS state for Fe(II) from magnetic measurements (vide infra). At 130 K the average Fe−N bond lengths are 2.07(3) and 2.08(3) Å for A and B sites respectively. There is a shortening of ca. 0.103 Å, reflecting a transformation of 50% of the HS Fe(II) atoms into the LS state. This correlates quite well with the small plateau observed in the magnetic properties (vide infra). At 80 K the system is fully in the LS state, the average Fe−N bond distances are 1.969(9) Å for site A and 1.976(9) Å for site B. Consequently, an additional shortening of ca. 0.103 Å occurs. The total shortening of the Fe−N bond length, 0.206 Å, is typical for a complete HS↔LS transition. The twelve characteristic angles of the $[FeN_6]$ core are close to 180° and 90°, and only a few of them change significantly with temperature. For example, N(1B)−Fe(1B)−N(2B) = 174.2(3) Å

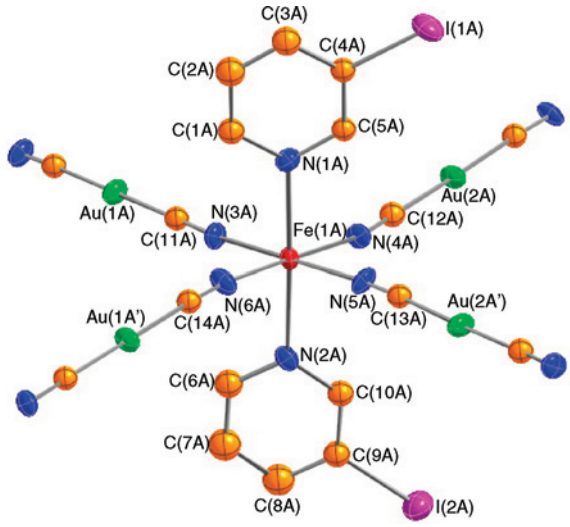

Figure 5. ORTEP representation of a fragment of **5** containing its asymmetric unit and atom numbering. Thermal ellipsoids are presented at 30% of probability.

at 293 K and 177.8(3) Å at 80 K, or N(1B)−Fe(1B)−N(4B) = 87.4(4)° at 293 K and 90.3(3)° at 80 K. The most significant changes are observed for the Fe−N−C(Au) angles, for instance, C(12A)−N(4A)−Fe(1A),C(14A)−N(6A)−Fe(1A),C(11B)−N(3B)−Fe(1B), and C(14B)−N(6B)-Fe(1B) change by 6.5, 3.8, 5.3, and 4.9°, respectively, between 293 and 80 K. Each $[Au(CN)_2]^-$ connects two iron atoms defining a 2D grid made, as in precedent examples, of sharing $\{Fe[Au(CN)_2]\}_4$ pseudosquare units, which make around 10.5 × 10.5 Å at 293 K and around 10.1 × 10.1 Å at 80 K. These 2D frameworks also associate by pairs (see Figure 2a and Figure 6) because of the formation of intense aurophilic interactions. These interactions are even more intense at low temperature with significant variations (ca. 0.037 Å and 0.079 Å in each step): Au(1A)···Au(2A) = 3.0426(8) Å (293 K), 3.016(2) Å (130 K), and 2.9924(5) Å (80 K); Au(1B)···Au(2B) = 3.1446(7) Å (293 K), 3.098(2) Å (130 K), and 3.0657(5) Å (80 K).

The separation between two consecutive double layers, [8.790(2) Å (293 K), 8.635(4) Å (130 K), and 8.548(2) Å (80 K)], is considerably larger than that observed for **1**−**4**. This larger separation favors the inclusion of a half-uncoordinated 3-Ipy molecule per iron atom (see Figure 6). The coordinated 3-Ipy rings of two adjacent double layers, [N(1A)−C(1A)−C(2A)−C(3A)−C(4A)−C(5A)] and [N(2B)−C(6B)−C(7B)−C(8B)−C(9B)−C(10B)], interact via π-stacking. Table 6 gathers the more significant C···C distances, those shorter than the sum of the van der Waals radius (ca. 3.7 Å). These distances clearly shorten when the system is cooled from 293 to 80 K (see Table 6). There are also short I···I interatomic distances, suggesting the occurrence of attractive intermolecular interactions. For instance, the I(1A)···I(2B) short contacts define infinite chains running along the 001 direction with I···I distances smaller than the sum of the van der Waals radius (ca. 4.30 Å); however, the I(1A)···I(1B) and I(2A)···I(1B) contacts are discrete. As in the case of C···C distances, the I···I contacts also shorten when moving from 293 to 80 K (see Table 6).

The included 3-Ipy guest molecules interact through the I(3) and N(7) atoms with other iodine atoms belonging to coordinated 3-Ipy molecules. A very weak temperature-dependent interaction between the I(3) and I(2A) atoms separated by ca. 4.30–4.17 Å is also noted (see Table 6). In contrast, a very strong intermolecular interaction observed between $N(7)^i$ [i = x, $^3/_2 - y$, $½ + z$] and I(2B) is characterized by a distance of 2.994(7) Å at 293 K and of 2.907(5) Å at 80 K (see red dotted lines in Figure 6, right panel). These values are well below the sum of the van der Waals distances [2.15 (I) + 1.54 (N) = 3.69 Å]. Furthermore, the angle C(9B)−I(2B)···N(7), where C(9B) is covalently bonded to the N(7), is almost linear 173.0(9)° at 293 K (174.3(8)° at 80 K). These facts indicate the formation of an acceptor–donor complex in which the guest 3-Ipy is the donor molecule through its N(7) atom while the 3-Ipy molecule coordinated to the Fe(B) site acts as an acceptor through the I(2B) atom. Indeed, the C(9B)–I(2B) bond distance, 2.128(11) Å at 293 K (2.118(10) Å at 80 K), is longer than that observed for the other 3-Ipy molecules not involved in such an interaction. The latter value has been found to be in the range 2.090(12)−2.023(8) Å at 293 K and 2.094(10)−2.043(4) Å at 80 K. The slightly elongated C(9B)−I(2B) distances are most likely due to the electron donation into the antibonding orbital associated with the C(9B)−I(2B)<···N(7) bond.

Magnetic and Calorimetric Properties. The thermal dependence of the product $\chi_M T$ for compound **1** at atmospheric pressure (10^5 Pa) is displayed in Figure 7a, with χ_M being the molar magnetic susceptibility and T the temperature. For **1**, $\chi_M T$ is equal to 3.73 cm^3 K mol^{-1} at 300 K, which is in the range of the values expected for an Fe(II) ion in the HS state. Upon cooling, $\chi_M T$ remains almost constant down to ca. 150 K; below this temperature, $\chi_M T$ changes sharply to attain a value of 1.90 cm^3 K mol^{-1} at 136 K. Then it remains practically constant down to ca. 50 K, and below this temperature a small but more marked decrease of $\chi_M T$ down to 1.35 cm^3 K mol^{-1} at 4 K is observed (see Figure 7b). These facts evidence that ca. 50% of the iron(II) atoms undergo a HS-to-LS spin transition. The warming mode denotes the occurrence of an asymmetric hysteresis loop 5 K wide with critical temperatures $T_c\downarrow$ = 140 K and $T_c\uparrow$ = 145 K.

Aimed at inducing a complete spin transition, we have investigated the magnetic behavior of **1** at pressures higher than 10^5 Pa (see Figure 7b). At 0.18 GPa this compound displays an almost complete two-step spin transition. At 300 K, $\chi_M T$ is ca. 3.66 cm^3 K mol^{-1}, and it decreases very slowly in the 300–240 K temperature range, then it decreases more rapidly to attain a value of 1.96 cm^3 K mol^{-1} at 145 K, which approximately corresponds to the center of an inclined plateau 25 K wide. A second less complete transition occurs in the 130–75 K temperature range. The $\chi_M T$ is equal to ca. 0.70 cm^3 K mol^{-1} at 75 K. The warming process does not match the cooling mode. In the 75–100 K temperature range, unexpectedly, $\chi_M T$ decreases to a value of 0.37 cm^3 K mol^{-1}. Then, for higher temperatures it increases rapidly to reach the plateau, which is less marked than in the cooling mode. Thus, in this lower temperature region $\chi_M T$ vs T plot defines an asymmetric hysteresis loop (ca. 40 K wide in its largest part) in a complete cooling-warming cycle. Once surpassed, the intermediate plateau $\chi_M T$ increases more rapidly again. In this temperature region, warming and cooling curves are quite similar, indicating that there is no appreciable hysteresis. The critical temperature is $T_c \approx 200$ K for the high temperature transition and $T_c\downarrow$ = 95.6 K and $T_c\uparrow$ = 122 K for the low temperature transition. The former temperature has been estimated by considering the temperature at 50% of conversion between 300 K and the plateau, whereas the latter have been estimated from the derivative of the curve. At a pressure of 0.26 GPa, the two-step spin transition shows a less marked plateau with T_c shifted to higher values: $T_c \approx$ 225 K for the high temperature transition and $T_c\downarrow$ = 131.5 K and $T_c\uparrow$ = 144 K for the low temperature transition.

Differential scanning calorimetry measurements for **1** were carried out at 10^5 Pa in the 130–300 K temperature range at a rate of 5 K/min. The thermal dependence of the anomalous heat capacity, ΔC_p, is shown in Figure 7a. An anomaly in the heat capacity appears centered at around $T_c\uparrow$ = 143.5 K (heating mode).

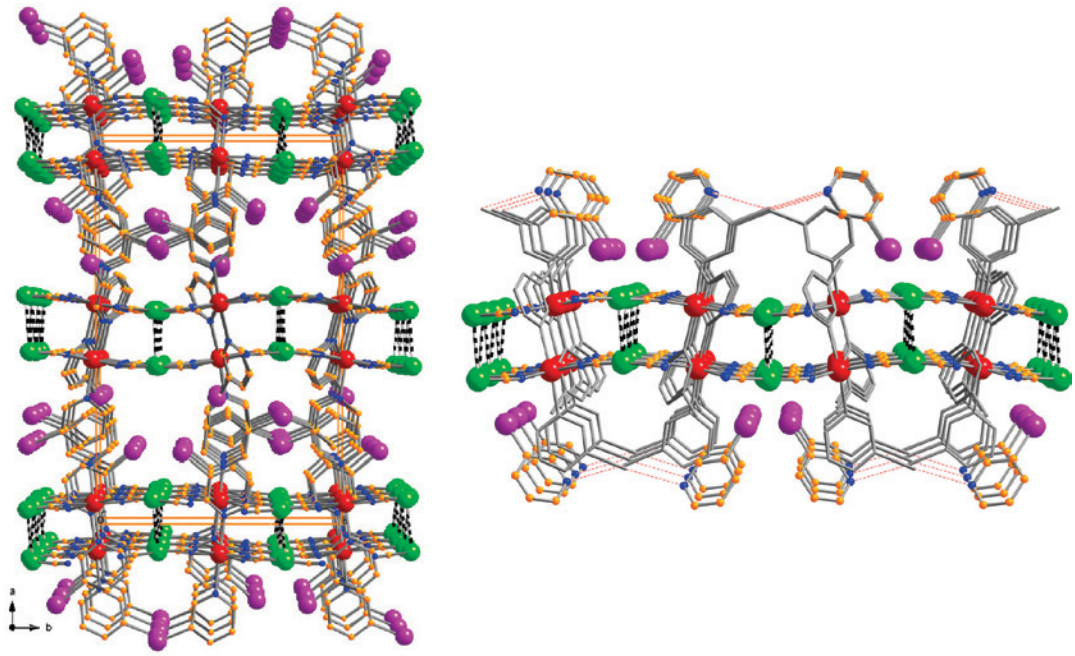

Figure 6. Left: view of the unit cell of **5**, emphasizing the stacking of six layers and the aurophilic interactions (dotted bars). Guest 3-Ipy molecules are not represented. Right: fragment of a double layer defined by the Fe(B) sites displaying the guest 3-Ipy molecules. Only the iodine atoms I(3) belonging to the guest have been represented as spheres. Dotted red lines denote the I(2B)···N(7) short interatomic contacts.

Table 6. Selected Intermolecular Contacts [Å] for **5**

	293 K	130 K	80 K
N(1A)···C(8B)	3.63(2)	3.60(5)	3.57(2)
N(2B)···C(3A)	3.66(2)	3.54(5)	3.48(2)
C(1A)···C(7B)	3.44(2)	3.42(6)	3.36(2)
C(2A)···C(6B)	3.46(2)	3.30(6)	3.34(2)
C(2A)···C(7B)	3.40(2)	3.33(5)	3.24(2)
C(4A)···C(9B)	3.65(2)	3.54(5)	3.463(14)
C(5A)···C(8B)	3.58(2)	3.57(5)	3.51(2)
I(1A)···I(1B)^{i}	3.909(2)	3.785(4)	3.6993(11)
I(1A)···I(2B)^{ii}	4.125(2)	4.064(4)	3.9820(11)
I(2A)···I(1B)^{iii}	4.047(2)	4.053(4)	4.0753(11)
I(2A)···I(3)^{iv}	4.305(2)	4.217(4)	4.1672(10)
I(2B)···N(7)^{ii}	2.994(7)	3.00(3)	2.907(5)

$^{i} = 1 - x, ½ + y, ³/₂ - z$; $^{ii} = x, ³/₂ - y, ½ + z$; $^{iii} = x - 1, y, z$; $^{iv} = -x, ½ + y, ½ - z$.

This value agrees well with the average critical temperature [$T_{av} = (T_c\downarrow + T_c\uparrow)/2 = 142.5$ K] observed from the $\chi_M T$ vs T plot. The derived thermodynamic parameters extrapolated to 100% transition are $\Delta H = 9.8 \pm 0.4$ kJ mol^{-1} and $\Delta S = 68.2 \pm 3$ J K mol^{-1}; these values are in the range of the values expected for cooperative spin transitions in Fe(II) compounds.a

The magnetic behaviors of **2**−**4** are characteristic of Fe(II) compounds in the HS state, $\chi_M T = 3.60$ (**2**), 3.64 (**3**), and 3.74 cm^3 K mol^{-1} (**4**) at 300 K. These $\chi_M T$ values are almost constant in the 300–50 K range of temperatures; at lower temperatures they display a typical behavior that is consistent with the occurrence of zero-field splitting in the S = 2 spin state. Figure 8 displays the magnetic properties of **3** as representative for the three compounds. $\chi_M T$ versus T plots for **2** and **4** are given in the Supporting Information. We have checked the possibility of inducing thermal spin transition on compounds **2** and **4** at higher pressures than 10^5 Pa; however, they do not show any spin transition at pressures less than 0.9 GPa.

The magnetic behavior of compound **5** is depicted in Figure 8. At 300 K, $\chi_M T$ is equal to 3.62 cm^3 K mol^{-1} and remains almost constant down to 203 K, then it decreases more rapidly, defining a relatively sharp spin transition that ends in an inclined plateau

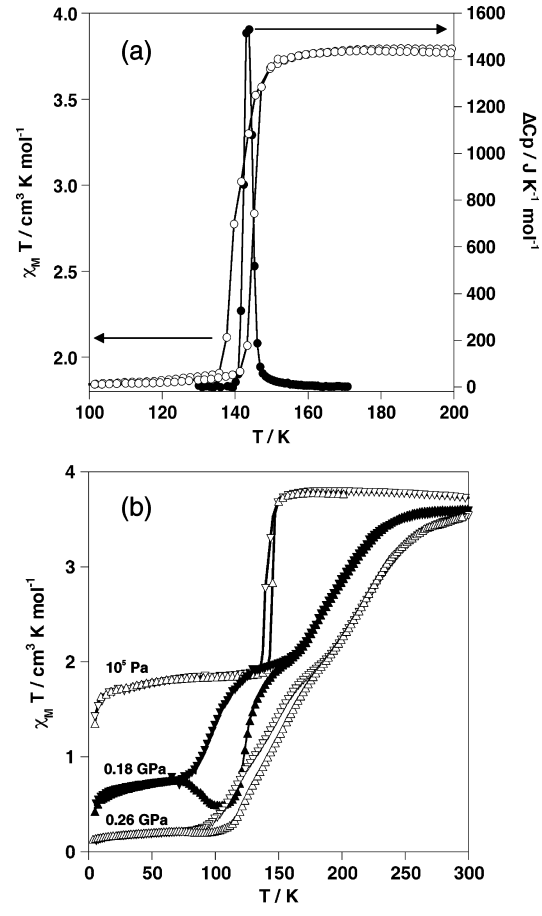

Figure 7. (a) An overlay of $\chi_M T$ and C_p versus T plots for **1** at ambient pressure (10^5 Pa). (b) Pressure dependence of the spin transition of **1** at 10^5 Pa and 0.18 and 0.26 GPa.

centered at 130 K with $\chi_M T \approx 1.79$ cm^3 K mol^{-1}. The critical temperature for this half-transition is $T_c^1 = 155$ K. Below this temperature a second more cooperative half-spin transition is

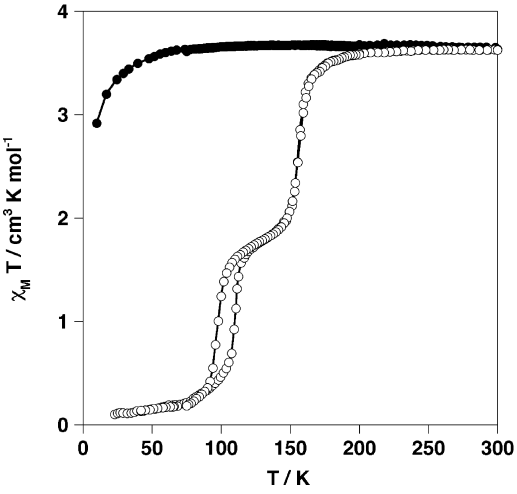

Figure 8. Magnetic Behavior of **3** (●) and **5** (○).

observed, and at 50 K the compound is essentially in the LS state ($\chi_M T = 0.14$ cm^3 K mol^{-1}). The warming procedure denotes the occurrence of a hysteresis loop ca. 13 K wide in the low temperature transition, whereas there is no detectable hysteresis for the high temperature transition. The corresponding critical temperatures for the latter transition are $T_c^2\downarrow = 97$ K and $T_c^2\uparrow = 110$ K. These low critical temperatures precluded estimating the thermodynamic parameters of the transition because the lowest attainable temperature in our calorimeter was ca. 120 K.

Discussion

In a previous paper we reported the synthesis and characterization of a closely related cyanide-bridged Fe(II)−Ag(I) bimetallic 2D Hofmann metal-organic frameworks.[13] Both, silver and gold derivatives afford two kinds of compounds, one formulated $\{Fe(3\text{-}Xpy)_2[M(CN)_2]_2\}$ (M = Ag or Au) and another which can be considered the 3-Xpy clathrate derivative of the former (X = 3-Brpy and 3-Ipy). Compounds $\{Fe(3\text{-}Xpy)_2[M(CN)_2]_2\}$ (M = Ag or Au) display very similar structures constituted of stacks of 2D coordination polymers organized by pairs. The separation between two layers in a pair is in the range 3.0–3.2 (Å), indicating the occurrence of strong argentophilic or aurophilic interactions. This separation strongly contrasts with that observed between two consecutive layers of different pairs, which is around 6 Å. In the silver clathrate derivatives, the layers are regularly distributed and no argentophilic interactions are observed. The 3-Brpy and 3-Ipy guest molecules are incorporated in the network separating the layers. This result strongly contrasts with the only clathrate obtained for the Au series. Interestingly, in this latter system the double layer structure remains after inclusion of the guest 3-Ipy molecules. Most likely, this is due to the well-known greater efficiency of the aurophilic interactions with respect to the argentophilic interactions. Apparently, inclusion of the guest 3-Ipy molecules cannot induce dissociation of the double layers but only increase separation between them.

Clear differences in the critical temperatures of the 3-Xpy gold and silver[13] spin crossover compounds have been observed. In the silver series the 3-Fpy and 3-Clpy derivatives undergo spin transition. The former displays a two-step transition with critical temperatures of 162 and 96 K, whereas the latter shows a 50% transition at 106 K. The 3-Brpy and 3-Ipy are HS in the whole range of temperature at 10^5 Pa. However, a rather incomplete continuous spin conversion in the 250–100 K temperature region with ca. 45% of Fe(II) ions remaining in the HS state at 4 K was observed for the 3-Ipy derivative at 0.43 GPa.

Concerning the gold series of compounds, only the 3-Fpy derivative is a spin crossover system. It undergoes a 50% spin transition at an average critical temperature of 142.5 K. This temperature is ca. 20 K less than the first half-transition observed for the homologous $\{Fe(3\text{-}Fpy)_2[Ag(CN)_2]_2\}$. At room temperature the crystal structure shows the occurrence of only one crystallographically different Fe(II) in the HS state. However, two crystallographically different but equally populated Fe(II) sites, one LS and the other HS, appear below the critical temperature. Application of relatively low pressures, between 0.18 and 0.26 GPa, induces a complete two-step spin conversion, which takes place at higher temperatures. Interestingly, in this pressure range the resulted two-step spin transition is similar to that observed for $\{Fe(3\text{-}Fpy)_2[Ag(CN)_2]_2\}$ at ambient pressure. The decrease observed for the $\chi_M T$ vs T curve in the 75–100 K interval at 0.18 GPa, in the warming mode of the hysteresis loop, could be at first sight an unexpected behavior because the LS state is stabilized as T increases. This fact cannot be explained in terms of thermodynamic considerations. Below 100 K, kinetics of the LS↔HS transformation is markedly slower than at higher temperatures. In these circumstances, the characteristic time to reach thermodynamic equilibrium may be longer than the elapsed time between consecutive measurements (in this experiment the scan rate was 1 K min^{-1} for the warming and cooling modes), consequently, thermal trapping of HS species may occur. In fact, in the cooling mode, the low temperature spin transition slows down gradually and ca. 19% of HS Fe(II) ions get blocked below 75 K. In the warming mode, due to the occurrence of thermal hysteresis, the spin conversion shows a positive shift of ca. 40 K. Hence, ca. 50% of the kinetically blocked HS iron(II) ions relaxes to the thermodynamically stable state in the 75–110 K temperature region, namely the LS state. At higher temperatures, normal thermal promotion from the LS state to the HS state takes place. The remaining $\{Fe(3\text{-}Xpy)_2[Au(CN)_2]_2\}$ compounds do not undergo spin transition even at pressures as high as 0.9 GPa.

Comparison of the spin transition behavior of both silver and gold families evidence a clear down-shift tendency of the critical temperatures when moving from silver to gold. This tendency has been previously noted for the two different series of isostructural compounds $\{Fe(pyrimidine)(H_2O)[M(CN)_2]_2\}\cdot H_2O$[6b] and $\{Fe(3\text{-}CNpy)_2[M(CN)_2]_2\}\cdot {}^2/_3H_2O$ (M = Ag and Au)[12c,d] where a decrease of the average critical temperature by ca. 52 and 62 K was observed, respectively. This effect can be understood in terms of the well-known relativistic effects observed for heavy atoms, which explain the much higher electron affinity of gold with respect to

silver.[16] In this respect, stronger electron withdrawing (polarizing) effect over the CN groups of the $[M(CN)_2]^-$ anions, and hence a poorer donor capacity of the nitrogen atoms for the gold derivative, should be expected. This should be reflected on the occurrence of shorter Au−C and longer CN−Fe bonds with respect the Ag counterpart. In fact, this is the case for the pyrimidine and 3-CNpy derivatives mentioned above. However, in the present case this tendency has been only noted for the Au−C bonds, which are shorter than the corresponding Ag−C bonds (see Tables 3 and 4).

Compound **5** represents a new evidence of clathration and, as in the previous $\{Fe(3\text{-}Xpy)_2[Ag(CN)_2]_2\}$ (X = Br and I) examples,[13] the clathrate compound undergoes a spin transition in contrast to its unclathrate counterpart. This is new evidence indicating that inclusion of 3-Xpy molecules in these coordination polymers favors the occurrence of spin crossover. In the case of **5** we have observed the formation of a strong charge-transfer donor–acceptor complex N···>I between the guest 3-Ipy molecule nitrogen atom and the iodine atom of the 3-Ipy coordinated to the Fe(B) site, thereby injecting extra electron density to it. Such type of supramolecular interaction is currently being investigated in the context of crystal engineering.[17] In particular, strong N···I interactions have been reported for the infinite chains 4,4′-bipyridine/1,4-diiodobenzene or diiodotetrafluorobenzene. For these two systems, the N···I distances (and interaction energy) are 3.032 Å (13.19 kJ mol^{-1}) and 2.851 Å (24.32 kJ mol^{-1}), respectively.[17a] In the case of **5**, the N···I distances, 2.994(7) at 293 K and 2.907(5) at 80 K, are more-or-less at halfway of the mentioned systems. So it is sensible to infer that this electron injection into the coordinated 3-Fpy group makes it a better donor, thereby increasing the ligand field strength in site Fe(B). In this respect, the magnetic data shows the occurrence of a two-step spin transition. At this point, one should stress that site Fe(B) would experience a spin state change at higher temperatures than site Fe(A). However, the crystal data clearly shows that the two crystallographically different iron(II) sites change the spin state simultaneously. In the middle of the plateau 50% of Fe(A) and Fe(B) sites are in the LS state and the other 50% are in the HS state. As observed for other examples, in the present case crystallographic measurements cannot distinguish between both states. Therefore, X-rays give us only an average picture of an ordered -LS-HS-LS- structure. Similar examples have been observed and discussed previously (see ref 18 and references therein). The effect of electronegativity on the transition temperatures discussed above for the unclathrate compounds also seems to be valid for the clathrate compounds. The critical temperatures of **5** are significantly smaller than the corresponding ones observed for the silver clathate compounds $\{Fe(3\text{-}Xpy)_2[Ag(CN)_2]\text{-}Ag(3\text{-}Xpy)(CN)_2]\}\cdot 3\text{-}Xpy$ (X = Br and I).

Acknowledgment. Financial support is acknowledged from the Spanish Directorate-General for Research Science and Technology (DGICYT, No. CTQ 2007–64727), the Generalitat Valenciana for research grant No. ACOMP/2007/110, and from the European Network of Excellence MAGMANET. A. B. G. thanks the Spanish MEC for a research contract (Programa Ramón y Cajal).

Supporting Information Available: CIF data for compounds **1** (at 293 and 120 K), **2**−**4**, and **5** (at 290, 130, and 80 K). Crystal data of compound **2**. Projection of the 3-Xpy rings along the N(1)−Fe−N(2) axis illustrating the bisection of the angles defined by the Fe−N(3)N(4) and Fe−N(5)N(6) for **1** and **3**. Crystal packing of compounds **3** and **4**. Magnetic behavior of compounds **2**, and **4**. This material is available free of charge via the Internet at http://pubs.acs.org.

IC701865K

(16) Jansen, M. *Angew. Chem., Int. Ed. Engl.* **1987**, *26*, 1098.

(17) (a) Walsh, R. B.; Padgett, C. W.; Metrangolo, P.; Resnati, G.; Hanks, T. W.; Pennington, W. T *Cryst. Growth Des.* **2001**, *1*, 165. (b) Lommerse, J. P. M.; Stone, A. J.; Taylor, R.; Allen, F. H *J. Am. Chem. Soc.* **1996**, *118*, 3108. (c) Metrangolo, P.; Neukirch, H.; Pilati, T.; Resnati, G *Acc. Chem. Res.* **2005**, *38*, 386. (d) Míngues Espallargas, G.; Brammer, L.; Sherwood, P. *Angew. Chem. Int. Ed* **2006**, *45*, 435.

(18) Moussa, N. O.; Trzop, E.; Zein, S.; Molnár, G.; Collet, E.; Gaspar, A. B.; Real, J. A.; Borshch, S.; Tanaka, K.; Cailleau, H.; Bousseksou, A. *Phys. Rev. B* **2007**, *75*, 054101.